Automated coronary artery tree segmentation in coronary CTA using a multiobjective clustering and toroidal model-guided tracking method

Hongwei Du [a,b], Kai Shao [b,c], Fangxun Bao [a,*], Yunfeng Zhang [b,c,**], Chengyong Gao [d], Wei Wu [e], Caiming Zhang [b,f]

[a] *School of Mathmatics, Shandong University, Jinan, Shandong 250100, China*
[b] *Shandong Provincial Key Laboratory of Digital Media Technology, Jinan, Shandong 250014, China*
[c] *School of Computer Science and Technology, Shandong University of Finance and Economics, Jinan, Shandong 250014, China*
[d] *School of Physics, Shandong University, Jinan, Shandong 250100, China*
[e] *Department of Cerebrovascular Diseases, Cheeloo College of Medicine, Shandong University, Jinan, Shandong 250012, China*
[f] *School of Computer Science and Technology, Shandong University, Jinan, Shandong 250101, China*

ARTICLE INFO

ABSTRACT

Background and objective: Accurate coronary artery tree segmentation can now be developed to assist radiologists in detecting coronary artery disease. In clinical medicine, the noise, low contrast, and uneven intensity of medical images along with complex shapes and vessel bifurcation structures make coronary artery segmentation challenging. In this work, we propose a multiobjective clustering and toroidal model-guided tracking method that can accurately extract coronary arteries from computed tomography angiography (CTA) imagery.

Methods: Utilizing integrated noise reduction, candidate region detection, geometric feature extraction, and coronary artery tracking techniques, a new segmentation framework for 3D coronary artery trees is presented. The candidate regions are extracted using a multiobjective clustering method, and the coronary arteries are tracked by a toroidal model-guided tracking method.

Results: The qualitative and quantitative results demonstrate the effectiveness of the presented framework, which achieves better performance than the compared segmentation methods in three widely used evaluation indices: the Dice similarity coefficient (DSC), Jaccard index and Recall across the CTA data. The proposed method can accurately identify the coronary artery tree with a mean DSC of 84%, a Jaccard index of 74%, and a Recall of 93%.

Conclusions: The proposed segmentation framework effectively segments the coronary tree from the CTA volume, which improves the accuracy of 3D vascular tree segmentation.

© 2020 Elsevier B.V. All rights reserved.

1. Introduction

Atherosclerosis is a disease in which the interior of arteries narrow due to plaque buildup, and it is a major etiological factor that results in coronary artery disease (CAD). CAD has the highest death rate in the world at present, with its morbidity and mortality increasing annually, which constitutes a serious threat to human health [1]. Coronary CTA is a robust noninvasive way of screening for arterial disease; CTA images can reveal the anatomical details of blood vessels more precisely than can magnetic resonance imaging (MRI) or ultrasound, and CTA is safer and faster than catheter angiography [2]. To effectively diagnose CAD, it is important to be able to construct computationally created 3-D models of arteries from CTA. These models are used to detect plaques, extract the centerline of coronary arteries and evaluate the degree of coronary artery stenosis [3]. Consequently, considerable research has been conducted to accurately visualize and quantify coronary arteries.

Coronary artery segmentation is a fundamental step in accurate vessel visualization and CAD assessment. A large amount of research has focused on segmenting vascular structures, and these studies have applied very different strategies. The existing methods of vascular segmentation can be broadly classified into three main categories: pattern recognition methods, model-based methods and tracking-based methods [4]. Pattern recognition methods include matching filter-based [5,6], mathematical morphology-based

---

* Corresponding author.
** Co-corresponding author.
  E-mail address: fxbao@sdu.edu.cn (F. Bao).

[7], region growing-based [8,9], artificial intelligence-based [10], and clustering-based [11,12] methods, among others. The majority of pattern recognition techniques focus primarily on the vascular segmentation of low noise retinal X-ray images, but these methods cannot achieve ideal results when applied to coronary CTA images with complex noise.

The model-based approaches track the vasculature by means of explicit vessel models. To improve the evolution speed along the vascular structure in the traditional level set method, Zhu et al. [13] presented a vascularity-oriented level set approach to prevent boundary leakage and adapt to intensity variations. This method was found to be superior to the traditional level set method. Sum and Cheung [14] presented a vessel extraction approach utilizing a level-set-based active contour that overcomes the inability of the existing models to handle nonuniform illumination. To accurately segment retinal vessels, Zhao et al. [15] first detected wide retinal vessels by the active contour method and then applied the region growing to capture thin vessels. However, the model-based methods are sensitive to the initialization contour and tuning the controlling parameters relies on experience. Li et al. [16] proposed the distance regularized level-set evolution (DRLSE) approach to eliminate the reinitialization procedure. Liu et al. [17] proposed a level-set model that did not require the generation of an initial contour or the manual setting of controlling parameters. However, this method suffered from boundary leakage problems and could not achieve an ideal result in dealing with vessel bifurcation [18].

In the tracking-based approaches, pixels analysis is used to detect vessel centerlines and boundaries that are orthogonal to the tracking direction. Tek et al. [19] detected the ostia points automatically and extracted the centerline of the coronary artery using a graph-based optimization algorithm with multiscale medialness filters. By analyzing the resulting vector field, Bauer and Bischof [20] presented a tube-detection approach based on gradient vector flow to extract the centerlines of tubular structures. Then, these centerlines were grouped into complete tree structures. In [21], an anatomical model of the complete heart was used to locate the seed points of coronary arteries. Then, the vessel tree of coronary arteries was extracted by matching a cylinder-like model in combination with depth-first search. These methods are able to effectively segment the connected vascular trees, but the tracking steps terminate early in low-contrast, variable intensity and noisy image situations [4]. Moreover, these methods did not utilize prior knowledge of the coronary artery shape; thus, they may not be applicable for following vessel structures that are distal to the initialization point [22].

Overall, accurate vessel segmentation still faces two major challenges. First, medical images generally have low contrast and contain complex noise types due to the limitations of physical imaging systems [23,24]. Intensity inhomogeneity, intensity nonuniformity, shading and bias fields can also be apparent in images obtained by different imaging modalities [25]. Second, vessel branching, variations in tubular radii, and the nonrigid geometry represent additional challenges to the problem of automated vessel segmentation [26]. Although tracking methods can guarantee good vascular connectivity [27], noise, low contrast and intensity inhomogeneity may adversely affect the visibility of details, which will reduce the accuracy and the reliability of vascular tracking [24].

To overcome these challenges, the literature includes a variety of vessel tracking methods based on enhanced filtering. In these studies, the vascular structure was first enhanced and then vessel tracking was performed. Hessian-based filtering [28], linear-based filtering [29], nonlinear-based filtering [30] and other tube-detection filters [31,32] are used to enhance the vascular structures and track vessels based on their centerlines or boundaries. Aylward et al. [33] applied an eigenvalue analysis of the Hessian for centerline extraction and presented dynamic-scale enhancements that

improve the processing effects under conditions with noise, branch points, and local singularities. Xu et al. [34] proposed an improved vessel centerline tracking approach combined with the recursive geometrical tracking method and the eigenvector of the Hessian used in Aylward and Bullitt [33]. To extract both normal and abnormal vessels and reconstruct tree structures on the basis of anatomical knowledge, Kitamura et al. [35] proposed a dimension reduction approach to train a tubular 3D object classifier based on Hessian analysis and applied the Markov random field framework to vascular structure segmentation. Zhou et al. [36] used a multiscale coronary response method to enhance and segment the heart region and a 3D dynamic balloon tracking method to extract the coronary artery trees. These segmentation methods enhance the vessel structures and effectively retain sharp vessel edges. However, because both the vascular and surrounding structure are enhanced during the enhancement step, the structures that exist around the vessels may also be mistaken for vessels in noisy images. During tracking, branching or crossing vessel structures may also cause some branches to be lost.

In this paper, we present an automated coronary tree segmentation approach for coronary CTA that uses a multiobjective clustering and toroidal model-guided tracking method. Primarily, we design a fuzzy C-means clustering (FCM) algorithm based on the fuzzy constrained histogram, called the multiobjective clustering method, which extracts vascular structures from complicated backgrounds as candidate regions. Further, we combine the nonlocal means (NL-means) denoising algorithm with the local fractal dimension (LFD) to reduce the influence of noise during candidate region extraction. Finally, we analyze the geometric features of the extracted candidate regions and apply a vessel tree-tracking method based on a toroidal model to segment the connected coronary artery tree structure. This method provides a solution for extracting 3D coronary artery trees from noisy, low-contrast medical images with intensity inhomogeneity that can automatically identify branching structures during tracking.

The main contributions of this paper can be summarized as follows. First, we propose a new arterial tree segmentation framework by integrating noise reduction, candidate region detection, geometric feature extraction, and coronary artery tracking techniques to perform accurate vessel extraction from coronary CTA. The proposed method improves the accuracy of 3D coronary artery tree segmentation. Second, we propose a method of coronary artery tracking based on a toroidal model that can extract entire coronary artery trees and solve most vessel bifurcation problems. Finally, we develop a multiobjective clustering method to distinguish vascular structures from complicated background regions, such as the lung and myocardium, and various image artifacts. In addition, we propose an NL-means denoising algorithm based on LFD to denoise medical images while preserving subtle vascular structures.

The remainder of this paper is organized as follows. Section 2 describes the clinical CTA data. Automated coronary artery tree segmentation using the multiobjective clustering and toroidal model-guided tracking method is presented in Section 3. Section 4 reports the experimental results, and Section 5 provides a discussion. Finally, conclusions are drawn in Section 6.

2. Clinical CTA data

The clinical coronary CTA data were retrospectively collected from the Department of Radiology, Cheeloo College of Medicine, Shandong University. The study protocol was approved by the Ethics Committee of the Cheeloo College of Medicine, Shandong University. The methods were carried out in accordance with the approved guidelines and regulations. All the images were real coronary CT angiography images from 100 consecutive patients. Among
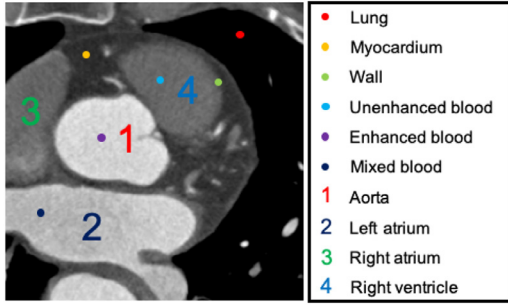
Fig. 1. Sketch map of tissue distribution in a coronary CTA image.

the collected cases, 93 patients were diagnosed with coronary stenosis, and the remaining 7 patients were normal.

CTA examinations were performed on a third-generation dual-source CT scanner (Somatom Definition Flash, Siemens Healthcare, Forchheim, Germany). All the scans were acquired during inspiratory breath hold, and the range was set from the apex to the base of the heart. The scanning parameters were as follows: orientation, axial; tube voltage, 120 kV; tube current, 400 mA; slice thickness, 0.7 mm; rotation time, 0.5 s; window width, 800 Hu; window level, 300 Hu; and image matrix, 512×512.

3. Methods

In this section, we propose an automatic segmentation method for performing blood vessel tree extraction from coronary CTA data that operates via noise reduction, candidate region extraction and vascular tree tracking. The method employs a multiobjective clustering algorithm and a toroidal model-guided tracking method to obtain the final coronary artery tree segmentation.

3.1. Multiobjective clustering

As shown in Fig. 1, coronary CTA slices usually contain lung, myocardium, blood and wall [37–39]. According to the contrast of the radiocontrast agent, blood can be divided into contrast-enhanced blood, a mixture of unenhanced and enhanced blood (mixed blood), and unenhanced blood [40]. The degree of blood enhancement is positively correlated with the concentration of the contrast agent [41]. In Fig. 1, the aorta contains contrast-enhanced blood; contrast-enhanced blood and mixed blood appear in the left atrium; and unenhanced blood flows in the right atrium and right ventricle. Coronary arteries usually have both enhanced blood and mixed blood.

To accurately extract vascular structures from this complicated background, we present an FCM clustering method based on fuzzy constrained histograms and utilize the NL-means denoising algorithm based on LFD to eliminate noise interference during vascular structures extraction.

3.1.1. Noise reduction

In general, medical CTA images usually include various types of noise because of various medical imaging factors. This noise has a negative effect on the target segmentation of medical images, especially on small coronary arteries. Therefore, noise reduction is an important step in coronary artery segmentation.

The majority of existing denoising methods are based on averaging the pixels in the image to achieve a denoising effect; however, this approach tends to cause the loss of image details during the denoising process. The NL-means algorithm [42] utilizes the redundant information in the image to filter out noise, and it preserves image details well. However, when the method incorrectly selects similar points, the details of image information will not
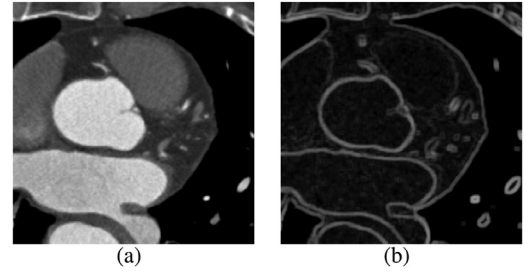

Fig. 2. Sketch map of a fractal dimension: (a) original noisy image; (b) corresponding fractal dimension image.
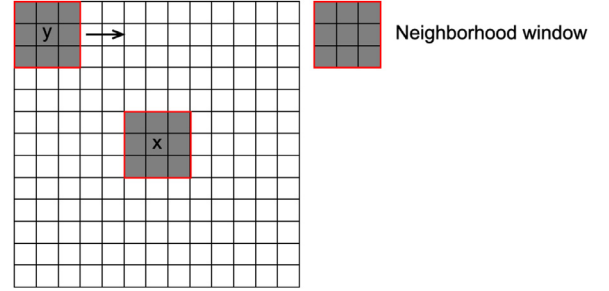

Fig. 3. The sliding process of the neighborhood window in the search window.

be preserved well, which is especially common in medical images with complex textures. Instead, a fractal can describe the spatial characteristic information of the image correctly. The LFD [43] is an important parameter that characterizes the amount of roughness in an image. As shown in Fig. 2, LFD can satisfactorily segment different texture regions in noisy CTA images. Thus, we propose a NL-means denoising algorithm based on LFD that combines LFD with the local mean to search for and correctly select similar points. This approach results in a better denoising effect. Here, we first introduce how to compute LFD and the fractal dimension for the images; then, we describe the NL-mean denoising algorithm based on LFD.

We can consider a CTA image as a curved surface in 3-D space, where the first two coordinates (x, y) represent the 2-D plane position and the third coordinate z is the pixel value. For a given image of size $M \times M$, we partition the 3-D space into $s \times s \times s$ boxes, where $r = M/s$. Suppose that the minimum and maximum values of image pixels in the grid (i, j) are in the box u and box v, respectively; then, $nr(i, j) = v - u + 1$ is the number of boxes required to cover the image in the grid (i, j). Further, the number of boxes required to cover the entire image is Nr:

$$Nr = \sum_{i,j} nr(i, j), \tag{1}$$

and the fractal dimension of the whole image D is

$$D = \lim_{r \to \infty} \frac{log(Nr)}{log(1/r)}. \tag{2}$$

LFD can be obtained by calculating fractal dimension of each image patch according to Eq. (2).

In Fig. 3, the large window is a search window centered on the target pixel x, and the two gray small windows are neighborhood windows centered on x and y, respectively. The neighborhood window centered on y moves within the search window, and each pixel x is computed as the weighted average of the pixels that have structures similar to x in the search window. Namely, given a noisy image v, the denoised image is:

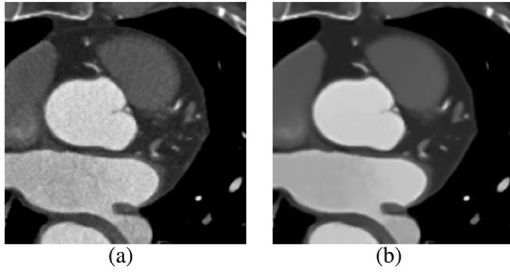$$u(x) = \sum_{y \in I} \omega(x, y) v(y), \tag{3}$$

Fig. 4. The denoised CTA image: (a) original CTA image slice; (b) denoised image.

Table 1
Quantitative results of our method under different noise levels in CTA.

Noise	Level	Index	Noisy	NL-mean	Our
Gaussian	0.01	PSNR	23.7745	25.2741	27.6304
		SSIM	0.3257	0.3840	0.4873
	0.02	PSNR	23.3517	24.7508	26.8351
		SSIM	0.3222	0.3783	0.4800
	0.04	PSNR	22.2479	23.3259	24.7558
		SSIM	0.3167	0.3780	0.4793
	Average	PSNR	23.1247	24.4503	26.4071
		SSIM	0.3215	0.3801	0.4822
Speckle	0.01	PSNR	30.2994	33.0542	34.4043
		SSIM	0.7898	0.8659	0.8877
	0.02	PSNR	27.3757	28.6147	30.7466
		SSIM	0.7121	0.7799	0.8148
	0.04	PSNR	24.5856	24.5905	25.7708
		SSIM	0.6330	0.6828	0.7214
	Average	PSNR	27.4202	28.7531	30.3072
		SSIM	0.7116	0.7762	0.8080

where the family of weights $\{\omega(x,y)\}_y$ depend on the similarity between x and y and satisfy the usual conditions, i.e., $0 \leqslant \omega(x,y) \leqslant 1$ and $\sum_y \omega(x,y) = 1$. I represents the pixels in the search window.

To better preserve image edges and complex textures during denoising, the first task is to search for the correct similar points for pixel x with the help of the LFD. The LFD can reflect the roughness of the image block. Therefore, the threshold T is used to filter out dissimilar image blocks based on LFD. Let $fd(x)$ be the fractal dimension of pixel x. When $|fd(x) - fd(y)| > T$, $\omega(x,y) = 0$; when $|fd(x) - fd(y)| \leqslant T$, the similarity as a decreasing function of the weighted euclidean distance:

$$\omega(x,y) = \frac{1}{Z(x)} e^{-\frac{\|fd(x)-fd(y)\|^2}{h^2}}, \tag{4}$$

where $Z(x)$ is a normalizing constant calculated as follows:

$$Z(x) = \sum_y e^{-\frac{\|fd(x)-fd(y)\|^2}{h^2}}, \tag{5}$$

where $fd(x)$ denotes a square neighborhood centered at pixel x. The parameter h acts as the filtering degree.

We present the denoising result to evaluate the effectiveness of the proposed method in Fig. 4. Fig. 4(a) is an original CTA image slice of coronary artery, while Fig. 4(b) shows the denoised CTA image result. Clearly, the proposed method preferentially suppresses image noise and effectively highlights the image details, which makes blood vessel extraction easier.

To validate the effectiveness of the proposed denoising method, the quantitative assessments Peak Signal-to-Noise Ratio (PSNR) and (Structural SIMilarity) SSIM are introduced to evaluate the denoising performance of our approach [44]. The random Gaussian noise and the random speckle noise are used to simulate noise in medical images [45]. In Table 1, we show quantitative results of our method under different noise levels in CTA. For example, 0.01 means that images are added Gaussian noise or speckle noise with mean 0 and variance 0.01. Compared with the NL-mean denois-

ing algorithm, the PSNR and SSIM of our method are improved by 1.9568dB and 0.1021 in terms of random Gaussian noise, respectively, the PSNR and SSIM of our method are improved by 1.5541dB and 0.0318 in terms of random speckle noise, respectively.

3.1.2. Coronary artery candidate region extraction

The gray values of the tissues on the CTA images accord with the Gaussian probability distribution, and FCM achieves good performance for processing Gaussian distribution data [46]. However, its fuzzification parameter m and cluster number c are usually obtained based on subjective experience. To be more specific, when the fuzzification parameter m is larger than the ideal value, the clustering results are generally not satisfactory, and when the fuzzification parameter m is smaller than the ideal value, the clustering result is similar to the result of the hard c-means clustering algorithm. Consequently, the parameter accuracy directly affects the clustering result. Therefore, we present an adaptive multiobjective vessel extraction method based on a fuzzy restrained histogram FCM clustering by optimizing the parameters m and c. The extracted blood vessels are considered as candidate regions of the coronary artery.

The cluster number c depends on total number of categories of the main tissues. The pixel values of each major tissue conform to a Gaussian probability distribution; therefore, the cluster number c can be determined by counting the number of histogram peaks. The main steps of the method are illustrated in Fig. 5. In particular, due to the large number of pixels in the background region, the visual effect of the histogram in the foreground region is not significant. In Fig. 5(b), we show only the histogram of pixels in the foreground region. First, the filtering operation is used to blur the histogram and filter out some interfering information (see Fig. 5(c)). Then, the parameter c is determined by calculating the number of peaks of the Gaussian fitting curve (see Fig. 5(d)).

Let x be the gray value in the image, $g(x)$ be the Gaussian fitting curve function for the gray-histogram of the original image, and $\{x_i, i = 1 \ldots n\}$ be a list of the points, where each x_i satisfies the condition below

$$\left.\frac{dg(x)}{dx}\right|_{x=x_i} = 0 \ and \ g''(x_i) < 0.$$

Then, we can define a functional $peaks(g(x))$ representing the number of the wave crest in $g(x)$, i.e.,

$$peaks(g(x)) = \int_{-\infty}^{\infty} \sum_{i=1}^{n} \delta(x - x_i) dx = n, \tag{6}$$

in which $\delta(x)$ is the Dirac delta function. Let $c = peaks(g(x))$ and $g_i(x)$ be the Gaussian curve fitting function for the gray-histogram of i clusters; then, the total error of all Gaussian curve fitting functions can be written as

$$Error = \sum_{i=1}^{c} \sum_{k=0}^{255} \left| \frac{g_i(k) - hist(k)}{hist(k)} \right| \tag{7}$$

where $hist(k)$ represents the pixel numbers of gray value k. The fuzzification parameter m depends on the similarity of the main tissue distribution to a normal distribution. The optimal parameter m is determined when the clustering error $Error$ is the minimum.

We propose an adaptive multiobjective FCM clustering algorithm based on fuzzy histogram constraints that can accurately extract candidate regions of the coronary artery. The parameter C is determined according to the histogram peak, and the parameter m is optimized according to the clustering error. Fig. 6 shows multiobjective FCM clustering results of a 2D denoised CTA slice; we can see that our method can separate six major tissues: lung, myocardium, enhanced blood, unenhanced blood, mixed blood and wall. The gray values of the tissues on the CTA images align with
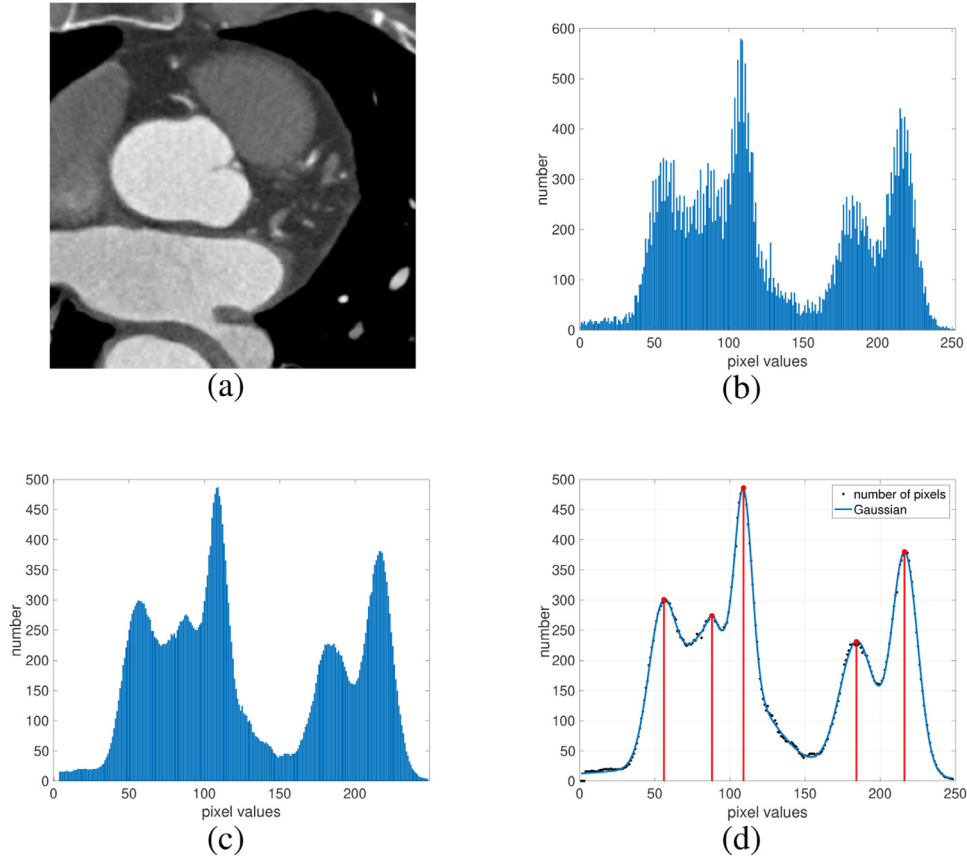
Fig. 5. Sketch map for the choice of the cluster number *c*: (a) original CTA image slice; (b) gradation histogram of the image foreground; (c) gradation histogram after the mean filter; (d) the curve fitted by the Gaussian function.
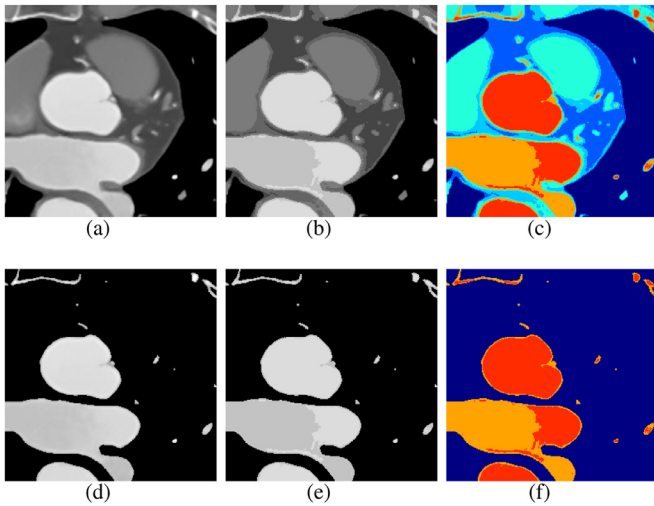
Fig. 6. The CTA image adaptive multiobjective clustering result: (a) denoised image; (b) multiobjective clustering results; (c) pseudo color image; (d) coronary artery candidate region; (e) clustering results of candidate region; (f) pseudo color image of candidate region.

the Gaussian probability distribution. To verify that the adaptive multiobjective clustering algorithm obtained reasonable parameters, Fig. 7 shows the Gaussian fitting residuals of each cluster histogram.

The Hounsfield unit (HU) scale is a quantitative scale for describing radiodensity. It is frequently used in CT scans, where its value is also termed the CT number. The CT number and gray value

meet the linear mapping relationship, which can be defined as

$$s_i = (z_{HU} - L) \times \frac{s_k - s_1}{W}, \tag{8}$$

where s_i is the gray value after mapping, z_{HU} is the original CT number, and $[s_1, s_k]$ is the range of gray values after mapping. In general, $s_k - s_1 = 255$. Let $[L, M]$ be the range of CT numbers; then, the window width $W = M - L$, and the window level can be expressed as $(M + L)/2$.

Under the operation of the professional physician, when threshold of the aortic region is close to peak enhancement (300 HU), the CT scanner will trigger a CT scan [47], so the optimal CT number of contrast-enhanced blood is 250–300 HU. Table 2 shows the CT numbers of different substances in cardiac CT. Coronary artery candidate regions are determined based on the CT number of enhanced blood and mixed blood.

3.2. Coronary tree tracking based on a toroidal model

In this section, we present an accurate coronary tree-tracking method based on a toroidal model. We assume that the blood vessel is a free-bending cylinder in 3-dimensional space. As shown in Fig. 8, the geometric features of the coronary cross-section in two adjacent CTA images correspond to two adjacent cross-sections of a freely curved cylinder. Therefore, the geometric features of the coronary cross-section of two adjacent CTA images can always find two cross-sections corresponding to one toroidal model.

We track the coronary artery tree from the candidate regions based on a toroidal model in three steps. First, we extract the geometric features of the candidate regions based on the toroidal model. Second, we estimate the coronary artery by analyzing the
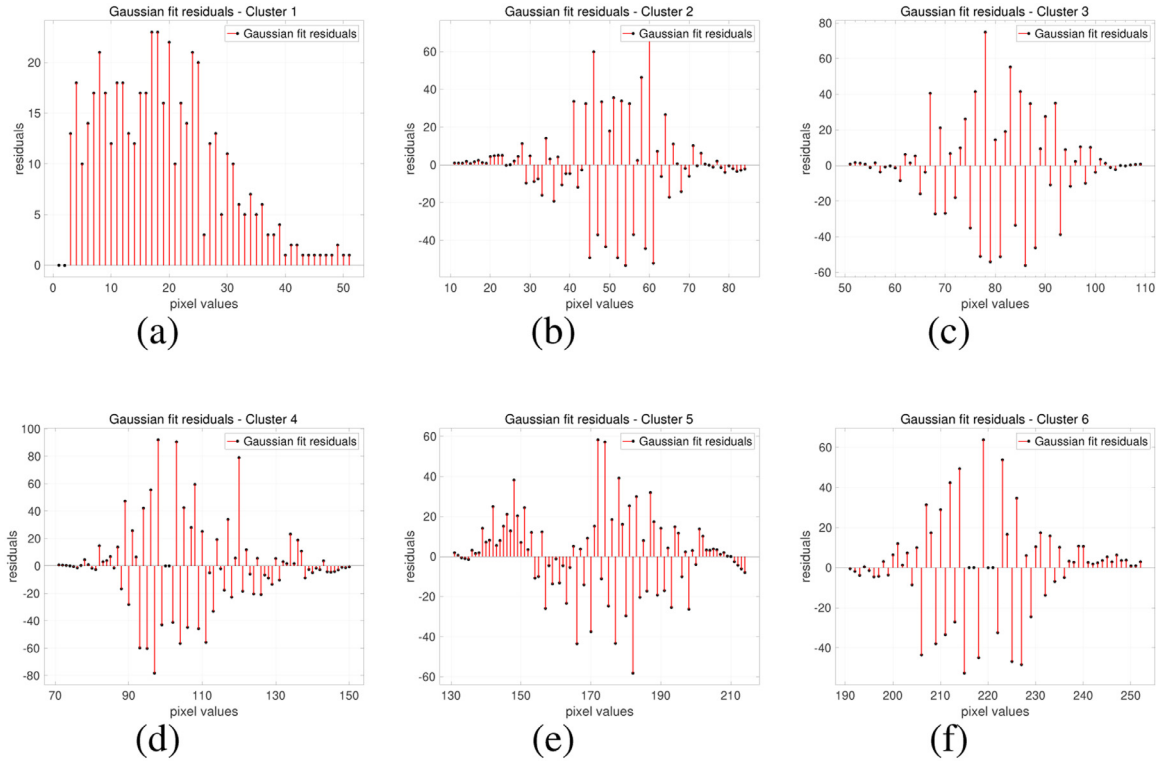
Fig. 7. Gaussian fitting residuals: (a) Gaussian fitting residuals of Cluster 1; (b) Gaussian fitting residuals of Cluster 2; (c) Gaussian fitting residuals of Cluster 3; (d) Gaussian fitting residuals of Cluster 4; (e) Gaussian fitting residuals of Cluster 5; (f) Gaussian fitting residuals of Cluster 6.

Table 2
CT number of different substances in cardiac CT.

Substance	HU
Air	1000
Lung[a]	700 to 600
Water	0
Muscle[b] (myocardium and wall)	+35 to +55
Blood (Unclotted)[c] [d]	+13 to +50
Mixed blood [41,47]	+200 to +250
Contrast-enhanced blood [47]	+250 to +300

[a] Page 379 in: Ella A. Kazerooni, Barry H. Gross 2004. Cardiopulmonary Imaging. 4. Lippincott Williams and Wilkins. ISBN 9780781736558.
[b] Page 83 in: Herbert Lepor (2000). Prostatic Diseases. W.B. Saunders Company. ISBN 9780721674162.
[c] Page 263 in: Robert Fosbinder, Denise Orth (2011). Essentials of Radiologic Science. Lippincott Williams and Wilkins. ISBN 9780781775540.
[d] Page 20.17 in: F W Wright (2001). Radiology of the Chest and Related Conditions. CRC Press. ISBN 9780415281416.

Fig. 8. Toroidal model: (a) hypotheses; (b) toroidal model.

features of candidate regions between adjacent slices. Finally, we trace the entire coronary artery tree using the depth-first search algorithm.

3.2.1. Geometric feature extraction

To accurately extract the coronary artery, we extract eight geometric features from the candidate regions and estimate their values in the toroidal model. The features include area S, perimeter C, centroid (x_m, y_m), major axis l_r, minor axis s_r, deformation degree Δe, centroid displacement Δd, and connectivity n. We also calculate the true value of each geometric feature.
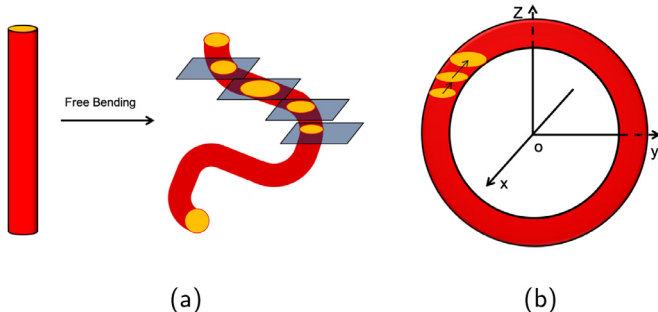
A torus can be defined parametrically by

$$
\begin{cases}
x(\theta, \varphi) = r \sin \theta \\
y(\theta, \varphi) = (R + r \cos \theta) \cos \varphi \\
z(\theta, \varphi) = (R + r \cos \theta) \sin \varphi
\end{cases}
\tag{9}
$$

where θ and φ are angles, r is the radius of the tube, and R is the distance from the center of the tube to the center of the torus.

Let $S(z)$ be the area of the candidate region of the zth slice.

$$
S(z) = \begin{cases}
2 \times \int_{\arcsin \frac{z}{R+r}}^{\arcsin \frac{z}{R-r}} z \cdot \csc^2 \varphi \sqrt{r^2 - (\frac{z}{\sin \varphi} - R)^2} d\varphi, \\
\qquad\qquad\qquad\qquad if \quad 0 < z < R - r \\
2 \times \int_{\arcsin \frac{z}{R+r}}^{\Pi - \arcsin \frac{z}{R+r}} z \cdot \csc^2 \varphi \sqrt{r^2 - (\frac{z}{\sin \varphi} - R)^2} d\varphi, \\
\qquad\qquad\qquad\qquad if \quad R - r < z < R + r
\end{cases}
\tag{10}
$$

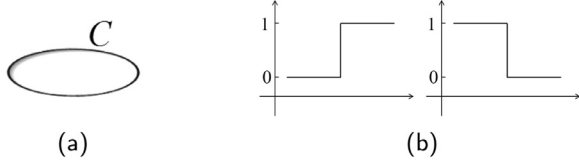In practice, the real area, S^{ground}, of the candidate region is determined by the statistical number of pixels. A schematic diagram for determining S^{ground} is shown in Fig. 9.

Fig. 9. Schematic diagram for determining the real area S^{ground} of the candidate region.

Fig. 10. Schematic diagram for determining the real perimeter C^{ground} of the candidate region.

Fig. 11. Schematic diagram for determining the real major axis $l_r^{ground}(z)$ of the candidate region.

Fig. 12. Schematic diagram for determining the real minor axis $s_r^{ground}(z)$ of the candidate region.
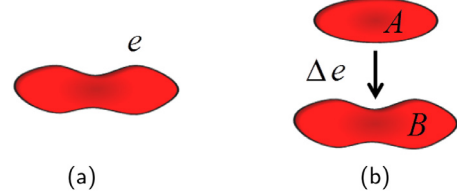
Fig. 13. Schematic diagram for determining the deformation degree $\Delta e(z)$ of the candidate region.

Fig. 14. Schematic diagram for determining the centroid displacement of the candidate region between two slices Δd.

Fig. 15. Schematic diagram for determining the connectivity between two slices n.

Let $C(z)$ be the perimeter of the candidate region of the zth slice.

$$C(z) = \begin{cases} 2 \times \int_{\arcsin \frac{z}{R+r}}^{\arcsin \frac{z}{R-r}} z \cdot \csc^2 \varphi \sqrt{1 + \frac{\cot^2 \varphi (1 - \frac{R}{z \csc \varphi})^2}{r^2 - (z \csc \varphi - R)^2}} d\varphi, \\ \qquad\qquad if \quad 0 < z < R - r \\ 2 \times \int_{\arcsin \frac{z}{R+r}}^{\Pi - \arcsin \frac{z}{R+r}} z \cdot \csc^2 \varphi \sqrt{1 + \frac{\cot^2 \varphi (1 - \frac{R}{z \csc \varphi})^2}{r^2 - (z \csc \varphi - R)^2}} d\varphi, \\ \qquad\qquad if \quad R - r < z < R + r \end{cases}$$
(11)

In practice, the real perimeter, C^{ground}, of the candidate region is determined by differential calculation. The schematic diagram for determining C^{ground} is shown in Fig. 10.

Let (x_m, y_m) be the centroid of the candidate region of the zth slice.

$$(x_m, y_m) = (\frac{x_1 + x_2 + \ldots + x_N}{N}, \frac{y_1 + y_2 + \ldots + y_N}{N})$$
(12)

In addition, let $l_r(z)$ be the major axis of the candidate region of the zth slice.

$$l_r(z) = \begin{cases} \sqrt{(R+r)^2 - z^2} - \sqrt{(R-r)^2 - z^2}, & if \quad 0 < z < R - r \\ 2\sqrt{(R+r)^2 - z^2}, & if \quad R - r < z < R + r \end{cases}$$
(13)

In practice, we transform the boundary points of the candidate region into polar coordinates with the centroid as the center and then calculate the lengths of all the line segments passing through the centroid to the boundary. The real major axis $l_r^{ground}(z)$ of the candidate region is the longest line segment. A schematic diagram for determining the real major axis, $l_r^{ground}(z)$, is shown in Fig. 11.
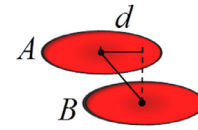
Let $s_r(z)$ be the minor axis of the candidate region of the zth slice, $s_r(z) = r$. In practice, we compute all the line segments perpendicular to the boundary of the major axis intersecting the can-
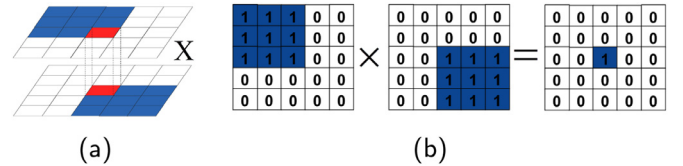
didate regions. The real minor axis, $s_r^{ground}(z)$, of the candidate region is the longest line segment. A schematic diagram for determining the real minor axis $s_r^{ground}(z)$ is shown in Fig. 12.

Let $e(z)$ be the deformation degree of the candidate region of the zth slice, $e(z) = \sqrt{l_r^2 - r^2}/l_r$, $0 < z < R + r$. The deformation degree of the candidate regions between slices A and B can be expressed as $\Delta e = |e_A - e_B|$. In practice, the real deformation degree can be defined as $\Delta e^{ground}(z) = \sqrt{l_r^{ground}(z)^2 - s_r^{ground}(z)^2}/l_r$. The schematic diagram for determining the real deformation degree $\Delta e^{ground}(z)$ is shown in Fig. 13.

Let $d(z)$ be the horizontal distance from the center of the tube to the center of the torus.

$$d(z) = \begin{cases} \sqrt{(R)^2 - z^2} & if \quad 0 < z < R - r \\ 0 & if \quad R - r < z < R + r \end{cases}$$
(14)

The centroid displacement of the candidate region between slices A and B can be expressed as $\Delta d = |d_A - d_B|$. In practice, $\Delta d^{ground} = \sqrt{(x_A - x_B)^2 + (y_A - y_B)^2}$. The schematic diagram for determining the centroid displacement of the candidate region between two slices Δd is shown in Fig. 14.

In addition to the above geometric features, connectivity is another important spatial feature for describing the candidate region relationships among slices. The schematic diagram for determining the connectivity between two slices n is shown in Fig. 15.

3.2.2. Estimating the coronary artery

We obtain the estimated and true values of the geometric features of the candidate region. The coronary arteries in the next
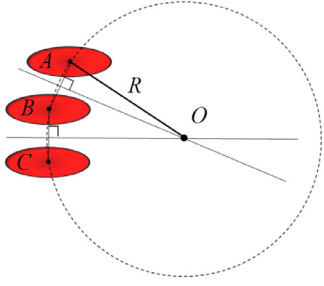
Fig. 16. Schematic diagram for determining the center of the torus R and the radius of the tube r.

slice are estimated based on the toroidal model. First, we obtain the center of the torus and the radius of the tube based on the geometric coronary artery features of three consecutive CTA slices. Then, the geometric characteristics of the coronary artery in the next CTA slice are predicted based on the toroidal model. Finally, we compare the geometric features of the predicted coronary artery with those of the candidate regions and identify the coronary artery from the candidate regions.

Fig. 16 shows a schematic diagram for determining the center of the torus R and the radius of the tube r. In Fig. 16, A, B and C are coronary arteries in three consecutive CTA slices, respectively. According to Eq. (11), we can calculate the centroid (x_A, y_A), (x_B, y_B), (x_C, y_C) of the coronary artery in slices A, B and C, respectively. The perpendicular bisectors of the coronary artery in A and B intersect with the perpendicular bisectors of the coronary artery in B and C at point O. In this case, let the distance from point O to any coronary centroid be R and $r = \frac{s_r(A) + s_r(B) + s_r(C)}{3}$. According to Section 3.2.1, the area $S_D^{predict}$, perimeter $C_D^{predict}$, major axis $l_D^{predict}$, centroid displacement $\Delta d_D^{predict}$ and the deformation degree $\Delta e_D^{predict}$ of the next coronary artery slice, D, can be obtained.

Under our hypothesis, the geometric feature of the adjacent coronary artery sections can be estimated using the toroidal model. Therefore, we can predict the geometric features of the next slice from the known three consecutive coronary slices. The geometric feature relationship between the slices can be described as follows:

$$\frac{S_C^{predict}}{S_D^{predict}} = \frac{S_C^{ground}}{S_D^{ground}} + \varepsilon_S; \frac{C_C^{predict}}{C_D^{predict}} = \frac{C_C^{ground}}{C_D^{ground}} + \varepsilon_C;$$
$$\frac{l_C^{predict}}{l_D^{predict}} = \frac{l_C^{ground}}{l_D^{ground}} + \varepsilon_l; \Delta d_D^{ground} - \Delta d_D^{predict} = \varepsilon_{\Delta d}; \qquad (15)$$
$$\frac{\Delta e_C^{predict}}{\Delta e_D^{predict}} = \frac{\Delta e_C^{ground}}{\Delta e_D^{ground}} + \varepsilon_{\Delta e}$$

where S_D^{ground}, C_D^{ground}, l_D^{ground}, Δd_D^{ground} and Δe_D^{ground} are the estimated true values of the geometric features of the coronary artery for the next slice. ε_S, ε_C, ε_l, $\varepsilon_{\Delta d}$ and $\varepsilon_{\Delta e}$ represent the parameter error of the geometric features.

3.2.3. Coronary tree tracking

The proposed coronary tree-tracking algorithm proceeds in a depth-first fashion. The goal is to build a segment chain $\alpha_0 \rightarrow \alpha_1 \rightarrow \alpha_2 \rightarrow \ldots$ to depict the vessel, where α_t represents a set of geometric features. Now we have $\alpha = \{C, l, S, \Delta d, \Delta e\}$ to estimate coronary artery in the previous section. From α_t to α_{t+1}, a feature extraction step and a prediction step are included.

The complete vascular tree tracking process is shown in Fig. 17. Assume that the current vessel segment is parameterized by α_t. The predictions for the next CTA slices exhibit two coronary artery regions, $\alpha_{t+1}^{(1*)}$ and $\alpha_{t+1}^{(2*)}$. We track one branch until we have traversed all the coronary arteries attached to that branch and then follow the next branch. By iterating over this procedure, we can build a tree to represent the tracking procedure, where the
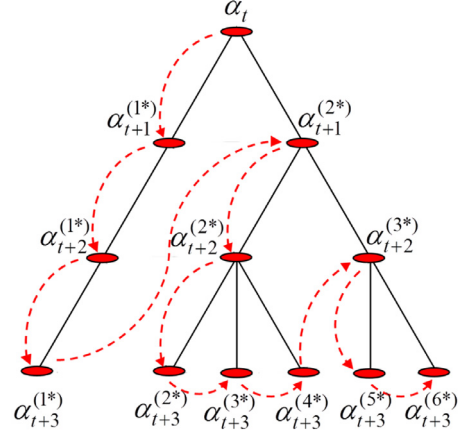
Fig. 17. An example of a coronary arterial tracking tree with a search depth of 3. Each node in the tree represents a coronary artery region, and the red dotted lines with arrows represent the search paths of the coronary tree.

leaves $\alpha_{t+3}^{(j*)}, j = 1, 2, \ldots 6$ represent possible vascular trajectories. The search depth is equivalent to the depth of the tracking tree.

The vascular tree-tracking algorithm is as follows:

4. Results

4.1. Qualitative results

The qualitative results are divided into denoising and segmentation evaluations. Fig. 18(b)–(e) illustrates the denoised images using four denoising approaches: the proposed denoising method, the NL-means denoising method, the median filter, and the Gaussian filter. The median filter is a classic nonlinear smoothing filter, but it is not effective at dealing with Gaussian noise. The Gaussian filter is a linear smoothing filter that suppresses Gaussian noise well. However, it does not preserve the edges and the details of the small vessels. The NL-means algorithm has a good capability for mitigating noise while simultaneously preserving the subtle local structures, which enables the vascular segmentation to extract precise arterial segments. However, when incorrect similar points are selected, the image detail information cannot be preserved well, especially in medical images with complex textures. Compared with the NL-means method, our method can obtain a more uniform vessel region. This result occurs because the presented denoising method searches for the correct similar points with the help of LFD.

To evaluate our denoising method, Fig. 19 demonstrates the clustering results after these different denoising methods. As shown in Fig. 19(b) and (e), our method preferentially suppresses the effects of noise on image clustering and produces the most competitive result compared to the other three methods. This result suggests that the proposed method improves segmentation performance by providing good vascular region detection.

Furthermore, we evaluated 2D segmentation performance with the active contour-based method, the level set-based method and the manual segmentation method. Considering the local image information, Li et al.'s approach [16] evolves the localized contours to segment objects with heterogenous feature profiles. To obtain robust and accurate segmentation results, Zhang et al. [49] presented a level-set based segmentation approach to integrate both boundary and region information. These approaches have achieved satisfying performance in segmenting the main objects of the image. However, for small objects such as the coronary artery, the initialization accuracy has a large impact on the segmentation results. In the manual segmentation method, three professional researchers
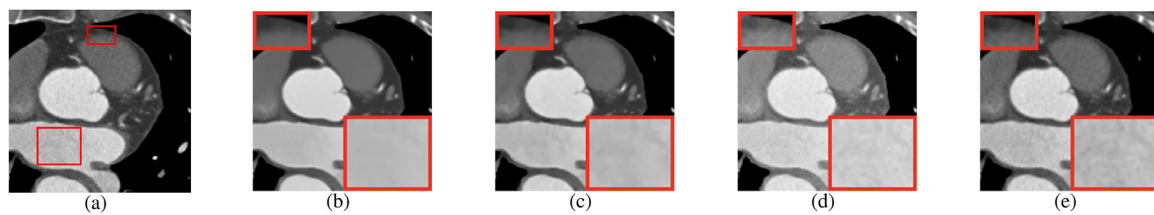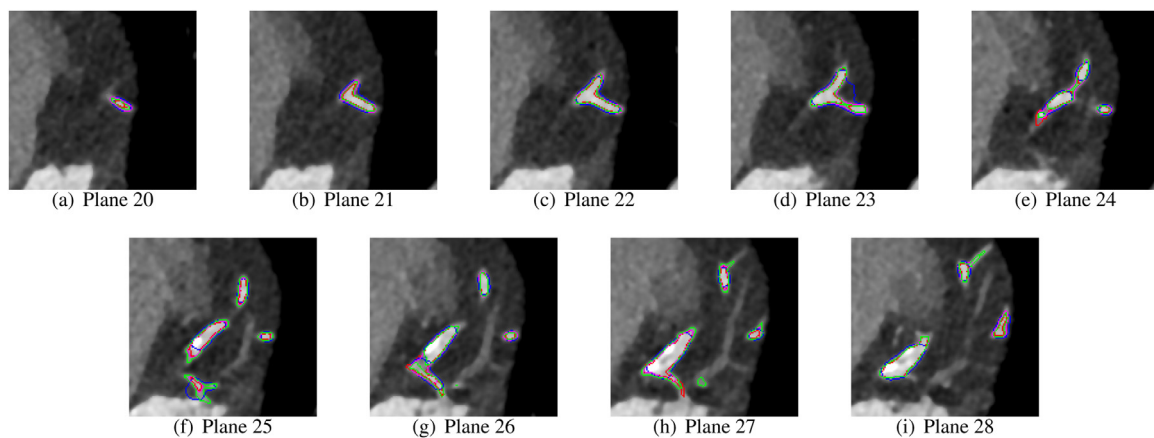
Fig. 18. Denoising results of different methods: (a) original slice; (b) our denoising method; (c) NL-means denoising method; (d) median filter; (e)Gaussian filter.
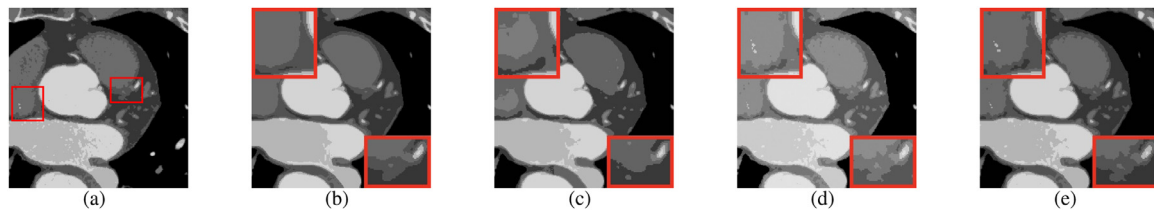
Fig. 19. Clustering results using different denoising methods: (a) clustering results on the original slice; (b) clustering results after our denoising method; (c) clustering results after the NL-means denoising method; (d) clustering results after median filtering; (e) clustering results after Gaussian filtering.

(a) Plane 20   (b) Plane 21   (c) Plane 22   (d) Plane 23   (e) Plane 24

(f) Plane 25   (g) Plane 26   (h) Plane 27   (i) Plane 28

Fig. 20. Segmentation results of some consecutive cross-sectional planes for CTA volume 05. Red indicates the manual-ground-truth segmentation, while green indicates the segmentation produced by our method. Blue and pink represent the segmentations produced by the methods of Li et al. and Zhang et al., respectively.

engaged in medical image analysis were trained to use 3D medical image processing software *MIMICS* to segment the coronary tree from CTA data. Prof. Wu Wei, an experienced radiologist, then inspected the manual segmented vascular tree to judge whether the results reflected the real facts in the original CTA images. We employed the authors' original implementations on our dataset for all the reference methods and obtained their best segmentation results by tuning the parameters manually. The resulting outputs on 8 consecutive cross-sectional planes are shown in Fig. 20. For the segmentation of small objects such as the coronary artery, Li et al.'s method and Zhang et al.'s method need manual parameter adjustments to achieve better segmentation results. As the parameters assigned to two methods improve, they achieve better segmentation results for regular objects. However, for irregular objects, Li et al.'s method cannot achieve perfect segmentation lines regardless of how many iterations it is allowed to execute. Overall, our approach does not match the manual segmentation completely; nevertheless, it is more competitive than the other two methods. Our method's advantage is that it identifies and segments most of the small branches and tiny vessels well.

To fully evaluate the performance of the proposed segmentation approach, we also compared the 3D reconstruction results of coronary artery by our segmentation method and those of the manual segmentation approach. To ensure a fair comparison, both our method and the manual segmentation 3D results were visualized

using 3*DMed* software. The resulting outputs from the CTA images of six representative patients are shown in Fig. 21. Compared with the manual segmentation results, our method detects more small branches and avoids discontinuous segments.
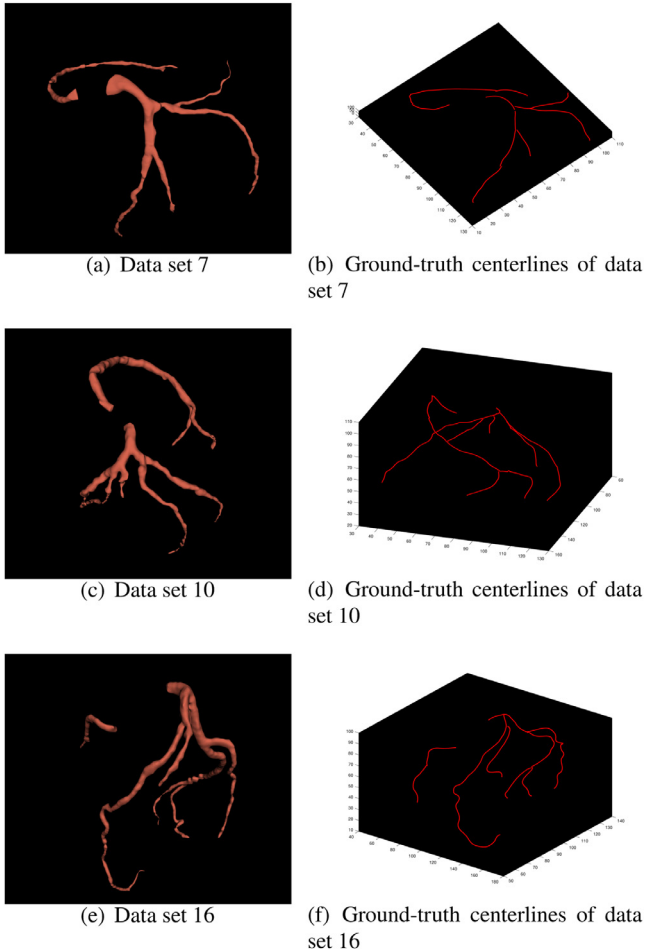
In addition, we performed the qualitative validation on the database provided as part of the Rotterdam Coronary Artery Algorithm Evaluation Framework [48]. The image database consists of 48 CT angiography data sets acquired using 64-row and dual-source CT scanners. It includes 18 training and 30 testing data sets with four reference vessels in each dataset. For eighteen of the data sets in the image database, the ground-truth centerlines drawn manually by three medical experts are publicly available (data sets 0–17), but they are not available for the remaining 30 data sets (data sets 18–47). Fig. 22 shows the coronary artery reconstruction results of three cardiac angiography data sets. According to the ground-truth centerlines, approximately 80–90% of the coronary vessels were segmented by the proposed approach.

4.2. Quantitative results

In addition to the qualitative results, we evaluated the proposed segmentation method through two types of metrics: distance-based and region-based metrics. For distance-based measures, we use mean absolute difference(MAD) to evaluate the mean difference between contour points of the automated segmentation
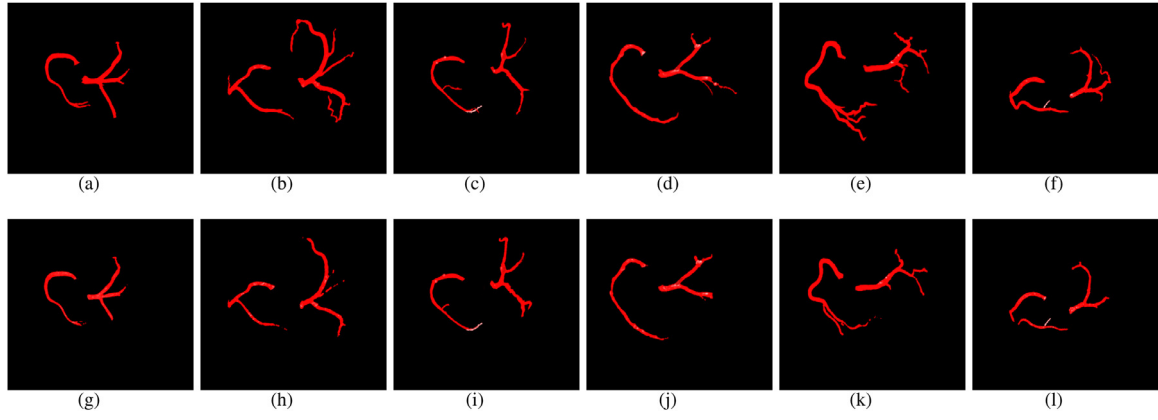
Fig. 21. Examples of both manual segmentation and the proposed method: (a)–(f) are the segmentation results of the proposed method, and (g)–(l) show the corresponding manual segmentation results.

(a) Data set 7   (b) Ground-truth centerlines of data set 7

(c) Data set 10   (d) Ground-truth centerlines of data set 10

(e) Data set 16   (f) Ground-truth centerlines of data set 16

Fig. 22. Coronary artery reconstructions of three cardiac angiography data sets.

$O_a = o_i^a | i \in 1, \ldots, N_a$ and the corresponding closest point o_j^g on the reference manual segmentation $O_g = o_j^g | j \in 1, \ldots, N_g$. The MAD computation is defined as in Zhang et al. [49]:

$$MAD = \frac{1}{N_a} \sum_{i=1}^{N_a} [\min_j ||o_i^a - o_j^g||_2] \tag{16}$$

where N_a and N_g are the numbers of points on the boundaries of the automated and manual segmentations, respectively. The seg-

mentation is more similar to the manual segmentation when MAD values are low.

For region-based measures, we use dice similarity coefficient (DSC) to measure the spatial overlap accuracy of the automated segmentation result compared to the reference segmentation. The DSC is computed by

$$DSC = \frac{2TP}{2TP + FP + FN} \tag{17}$$

where TP, FP, and FN denote true positives (the number of vessel pixels correctly identified), false positives (the number of nonvessel pixels incorrectly identified as vessel pixels), and false negatives (the number of vessel pixels that are not identified as vessel pixels), respectively. The DSC ranges from 0 to 1, with 1 denoting complete overlap. The DSC is suitable for quantifying the performances of the two segmentation methods.

We computed the overlap between the two polygons using the Jaccard index. The formula for calculating Jaccard index between the ground truth and segmentation result is

$$Jaccard = \frac{TP}{TP + FP + FN} \tag{18}$$

For highly overlapped segmentations, the Jaccard index approaches one, and the index approaches zero between two irrelevant images.

We also quantified the segmentation performance using *Precision* and *Recall*. These measures are defined as follows:

$$Precision = \frac{TP}{TP + FP} \tag{19}$$

$$Recall = \frac{TP}{TP + FN} \tag{20}$$

As shown in Fig. 23, we evaluated the proposed coronary tree segmentation method using five performance metrics and compared it to the reference methods. Our method obtained the best numerical results with regard to MAD, DSC, Recall and Jaccard, suggesting that our segmentation method is accurate and effective at dealing with coronary trees extraction from CTA images. According to the performances of the reference methods, we note that Zhang et al.'s approach obtained the highest SP values, which shows that this method is superior for detecting nonvessel regions, while Li et al.'s method resulted in the worst segmentation performance with regard to DSC, Jaccard and Precision but achieved fair results for MAD. This result occurred because Li et al.s method utilizes distance regularization and external energy to drive the contour motion toward the vessel boundary, which provides relatively accurate vessel tree contours, but the small vessels at bifurcation or crossing points are not considered.

(a) MAD

(b) DSC

(c) Recall

(d) Jaccard
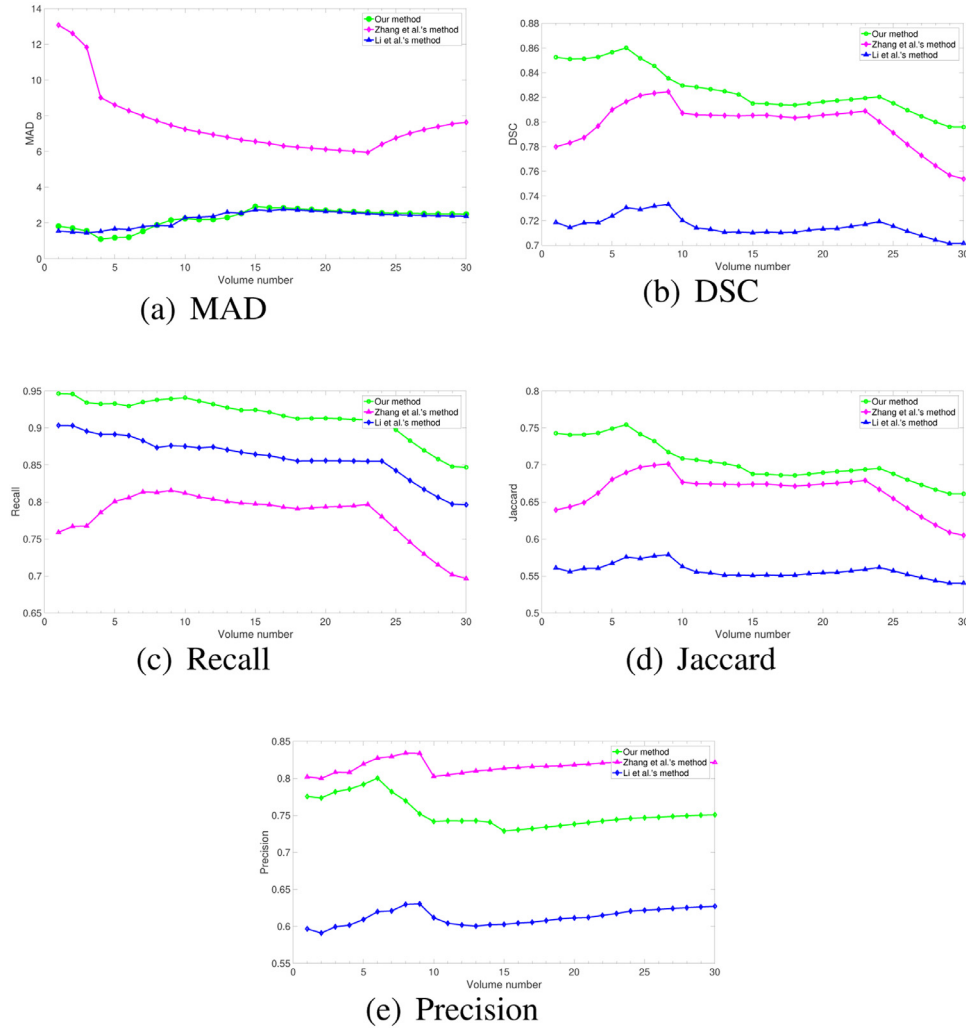
(e) Precision

Fig. 23. The segmentation performance measured by MAD, DSC, Recall, Jaccard and Precision.

Table 3

The segmentation performance measured by MAD, DSC, Recall, Jaccard and Precision.

Methods	MAD	DSC	Recall	Jaccard	Precision
Han et al. [50]	8.5392 ± 2.0374	0.7225 ± 0.0589	0.7476 ± 0.0449	0.6614 ± 0.1023	0.8016 ± 0.0992
Yu et al. [51]	12.1582 ± 2.5076	0.8048 ± 0.0995	0.8258 ± 0.1040	0.7258 ± 0.0807	0.8031 ± 0.0578
Shen et al. [52]	14.9851 ± 3.8697	0.8066 ± 0.1009	0.8300 ± 0.0666	0.6759 ± 0.0593	0.7502 ± 0.0605
Our method	3.8980 ± 0.7269	0.8217 ± 0.1392	0.9316 ± 0.0690	0.7810 ± 0.0710	0.8614 ± 0.0668

The proposed approach is also compared with the popular 3D object segmentation frameworks, a fast seed detection for automatic vessel tracking [50], a 3D densely-connected volumetric convolutional neural network (DenseVoxNet) [51] and a 3D fully convolutional network (FCN) [52]. Han et al. [50] proposed a fast seed detection for automatic tracking of coronary arteries in coronary CTA. However, this method does not solve the problem of vascular bifurcation. Yu et al. [51] used DenseVoxNet to automatically segment vascular structures from 3D datas. However, DenseVox does not consider long-range inter-node dependencies in the artery tree or the tree structure underlying in the artery tree. Shen et al. [52] presented a joint framework for coronary CTA segmentation based on 3D FCN. As the segmentation is applied to every single voxel of the coronary CTA volume, the network is extremely sensitive to local perturbations. Therefore, the results suffer from a significant amount of false positives and false negatives. According to

Table 3, the proposed coronary artery tree segmentation method achieved the most competitive results.

5. Discussion

We describe the effects of parameter variations, the computational cost and the bifurcation problem in this section.

5.1. Effects of clustering parameters

In the FCM clustering method, the cluster number c and fuzzification parameter m are two key parameters because they affect the accuracy of the final segmentation results. Fig. 24 shows the effect of varying the clustering parameter c on the clustering performance. When c is too small, some tissues will be merged. Conversely, when c is too large, there will be a redundant "transition
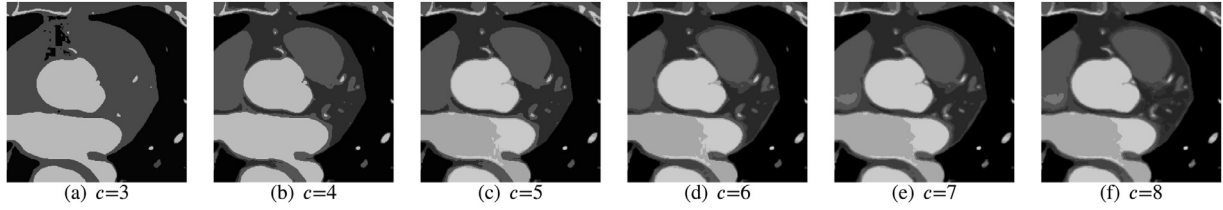
Fig. 24. The effects of varying the clustering parameter c on the clustering performance.
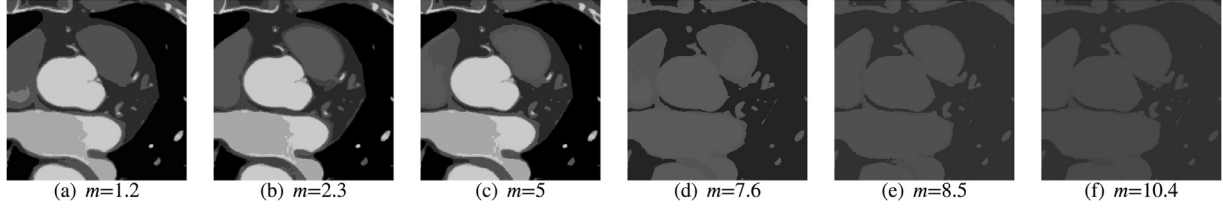
(a) $c=3$ (b) $c=4$ (c) $c=5$ (d) $c=6$ (e) $c=7$ (f) $c=8$

Fig. 25. The effects of varying the clustering parameter m on the clustering performance.

(a) $m=1.2$ (b) $m=2.3$ (c) $m=5$ (d) $m=7.6$ (e) $m=8.5$ (f) $m=10.4$

(a) Area Error   (b) Deformation Error   (c) Distance Error   (d) Major Axis Error   (e) Perimeter Error

(f) Area Error   (g) Deformation Error   (h) Distance Error   (i) Major Axis Error   (j) Perimeter Error
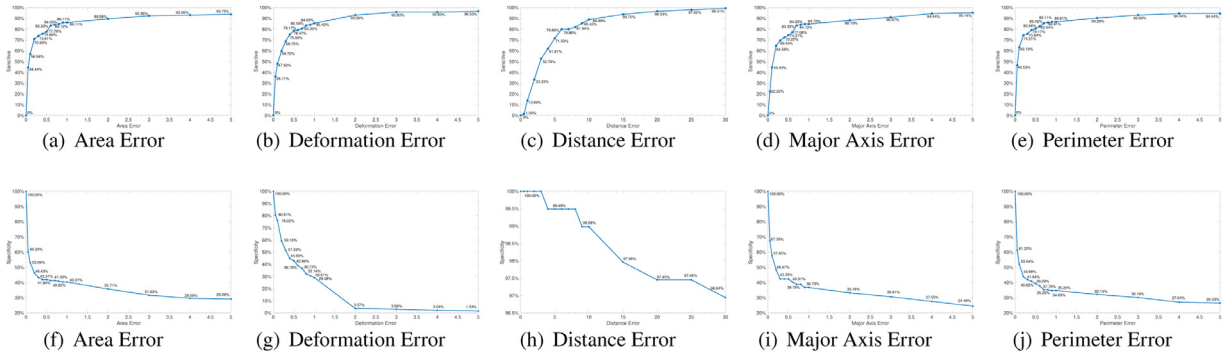
Fig. 26. The effect of varying the geometric feature error parameter on the coronary tree-tracking performance.

zone" between the two adjacent main tissues. In our method, we obtain c by counting the number of histogram peaks. In Fig. 24, we used $c = 6$, which works well for separating the lung, myocardium, wall, unenhanced blood, mixed blood and enhanced blood. Fig. 25 illustrates the effect of varying the parameter m on the clustering performance. When m is too large or too small, the clustering results are generally unsatisfactory.

5.2. Effects of geometric feature error parameters

Five types of errors, (perimeter error ε_C, area error ε_S, major axis error ε_l, distance error $\varepsilon_{\Delta d}$ and deformation error $\varepsilon_{\Delta e}$) determine the accuracy of coronary tree tracking. We employed the metrics *Sensitivity* and *Specificity* to evaluate the effects of geometric feature errors on coronary tree tracking. *Sensitivity* is defined as the proportion that the positives are correctly identified. *Specificity* is defined as the proportion that the negatives are correctly identified. High *Sensitivity* means the model has a low misrecognition rate. High *Specificity* corresponds to a lower false recognition rate. These measures are expressed as follows:

$$Sensitivity = \frac{TP_{error}}{P_{error}} \qquad (21)$$

$$Specificity = \frac{TN_{error}}{N_{error}} \qquad (22)$$

where TP_{error} represents the number of correctly identified coronary regions, TN_{error} is the number of correctly identified noncoronary regions, P_{error} denotes the number of coronary regions among all candidate regions and N_{error} is the number of noncoronary regions among all candidate regions.

Fig. 26 shows the effect of varying the geometric feature error parameters on coronary tree-tracking performance. We noted that *Sensitivity* increases as the geometric feature error increases, but *Specificity* is the reverse. Distance error $\varepsilon_{\Delta d}$ has the greatest influence on the coronary tree-tracking algorithm, followed by area error ε_S, perimeter error ε_C and major axis error ε_l, while deformation error $\varepsilon_{\Delta e}$ has the smallest influence on the algorithm performance.

5.3. Computation time analysis

Experiments were performed on the MATLAB R2017b platform using a computer equipped with an Intel Core i7 2.2 GHz CPU with 16 GB of RAM. Each patient has approximately 200 to 500 CTA slices, and the size of each CTA slice is 512×512. For each 2D slice, the average computational time for the FCM clustering algorithm was 1.05 s. The proposed vascular tracking algorithm requires approximately 556.5 s for the coronary tracking of the CTA volume ($512 \times 512 \times 350$) of a patient, with an average of 1.59 s to process a 2D slice. When the number of iterations was set to 300, Li et al.'s method [16] and Zhang et al.'s method [49] achieve near-convergence for most coronary arteries. In this situation, the two methods require approximately 9.16 s and 6.4 s, respectively, for processing a coronary artery region. Note that automatic coronary tree segmentation has been a challenging problem to date. The goal of this study is to minimize the need for human interaction. Our proposed segmentation method can track the entire coronary artery tree while requiring only one human interaction, and it provides superior performance in extracting the vascular tree.
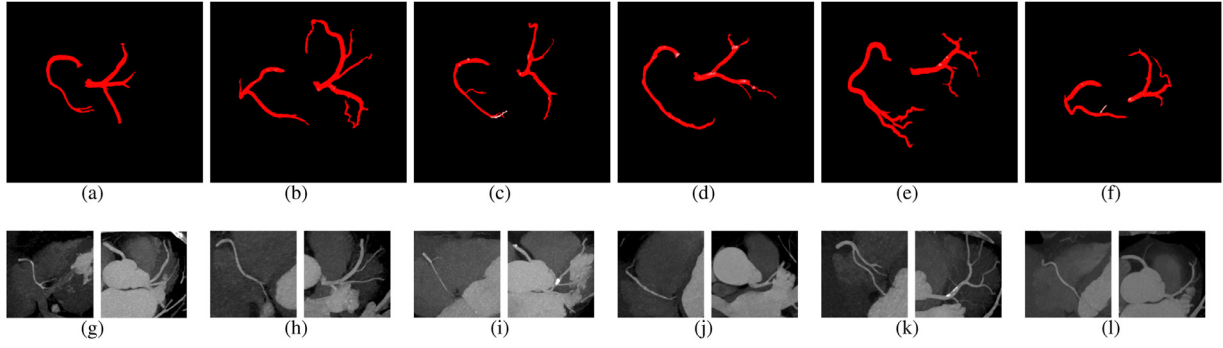
Fig. 27. (a)–(f) Segmented arteries from the proposed method are shown for CTA datasets; (g)–(l) MIP views of the datasets.

5.4. Bifurcation problem

One review study [53] states that bifurcation detection remains a challenging task in automated blood vessel segmentation, and only a handful of existing papers are specifically dedicated to bifurcation detection [54–56]. Baboiu et al. [56] presented a simple algorithm for directly detecting blood vessel bifurcation points through a comprehensive scale-space analysis of vascular bifurcations. This algorithm builds a simple bifurcation-ness filter with good sensitivity based on a simple scale-space conversion of the original image. Generally, to address the patient-specific vascular tree modeling problem, an initial segmentation step that produces a 3D segmented volume must be followed by a separate branch detection scheme. Later, it is used to construct a vascular tree model and sometimes followed by external mesh editing and further modeling [57–59]. In this study, we propose a novel vascular detection method based on a toroidal model. Our method parameterizes the geometric features of extracted candidate regions and then constrains the geometric parameters based on a toroidal model to finally detect the vascular branch structure.

To intuitively reflect the performance of our method in the detection of vascular branches, we compared the segmentation results using maximum intensity projection (MIP) [60] views. MIP is a computer visualization method for projecting three-dimensional spatial data onto a visual plane. Fig. 27 illustrates a 3D visualiza-

---

Algorithm 1 NL-mean denoising algorithm based on LFD.

Input: Original CTA volume $v(x, y, z(x, y), d)$, the size of a CTA slice is $M \times M$, x, y represent the row and column coordinate of the image slice respectively, $z(x, y)$ is grey value, d is the number of image slices;

Output: Denoised CTA volume, $u(x, y, z(x, y), d)$;

1: initialize the size of search window is $S \times S$, search step is 1;
2: **for** t=1:d **do**
3:     **for** $x = 1 : M$ **do**
4:         **for** $y = 1 : M$ **do**
5:             **for** $i = 1 : S$ **do**
6:                 **for** $j = 1 : S$ **do**
7:                     **if** $|fd(x, y) - fd(i, j))| \leqslant T$ **then**
8:                         compute $\omega(i, j)$ by Eq. 3;
9:                     **end if**
10:                 **end for**
11:             **end for**
12:         compute $z(x, y)$ by Eq. 4;
13:         **end for**
14:     **end for**
15:     obtain the denoised CTA slice $u(x, y, z(x, y))$;
16: **end for**
17: obtain the denoised CTA volume $u(x, y, z(x, y), d)$;

Algorithm 2 Coronary artery candidate region extraction algorithm based on fuzzy histogram constraints.

Input: Denoised CTA volume $u(x, y, z, d)$, the size of a denoised CTA slice is $M \times M$, x, y represent the row and column coordinate of the image slice respectively, z is grey value, d is the number of image slices;

Output: Candidate region volume, $R(x, y, z, d)$;

1: **for** t=1:d **do**
2:     determine the cluster number c by Eq. 6;
3:     **for** m=0:0.1:5 **do**
4:         perform FCM clustering algorithm on the denoised image u(x,y,z) based on the clustering parameter c and m;
5:         compute the clustering error $Error$ by Eq. 7;
6:     **end for**
7:     determine the fuzzification parameter m when the clustering error $Error$ is the minimum;
8:     obtain the clustering result of a denoised CTA slice;
9:     obtain candidate region $u(x, y, z)$ based on HU intensity values of contrast-enhanced blood and mixed blood;
10: **end for**
11: obtain Candidate region volume $u(x, y, z, d)$;

Algorithm 3 Coronary tree tracking based on a toroidal model.

1: Artificial marking of coronary artery regions α_{t-2}, α_{t-1}, α_t in three consecutive CTA slices A, B and C;
2: According to the coronary artery from the three previous consecutive slices, R and r are determined, and the thickness between slices d is known. Then, the geometric features of coronary artery $\alpha_{t+1}^{predicted*}$ in the next slice D are predicted;
3: The geometric features of the predicted coronary artery $\alpha_{t+1}^{predicted*}$ are compared with those of the candidate regions to identify the coronary artery regions α_{t+1}^{j*};
4: When more than two coronary artery regions $\alpha_{t+1}^1, \alpha_{t+1}^2, \ldots$ are identified, we repeat steps 2-3 to track one branch, and the origin of the other branches are reserved to be pursued later;
5: If the coronary artery is not identified, we terminate the current branch tracking and move to the next branch;
6: The above steps are repeated until all the branches have been searched.

---

tion of the proposed approach and MIP views of the dataset. By comparing our results with the MIP results, our method can detect the main branches of the coronary artery.

6. Conclusion

In this paper, we presented a new segmentation framework for 3D vascular trees and demonstrated its efficacy for coronary CTA

segmentation. Our NL-means denoising algorithm based on LFD removes the influence of noise from the segmentation of vascular small branches. The FCM clustering method based on fuzzy histogram constraints can distinguish vessels from the surrounding tissues. The automatic 3D coronary tree-tracking method based on a toroidal model solves the bifurcation problem. We validated the results both qualitatively and quantitatively. Our method outperformed the compared state-of-the-art segmentation methods in terms of DSC, Jaccard and Recall, achieving an average improvement of 5%. The comparison to manual segmentations suggests that our method has potential for use in computer-aided diagnostic systems that might both enhance the radiologist's operational efficiency and help improve diagnostic confidence. In the future, we are going to use the segmented coronary tree algorithm in machine learning frameworks to measure the degree of branch stenosis and detect calcification and plaques.

Declaration of Competing Interest

Authors declare that they have no conflict of interest.

Acknowledgments

References

[1] S. Waxman, F. Ishibashi, J.E. Muller, Global, regional, and national age-sex specific all-cause and cause-specific mortality for 240 causes of death, 1990–2013: a systematic analysis for the global burden of disease study 2013, Lancet 385 (9963) (2015) 117–171.

[2] S. Nemoto, [diagnostic imaging of carotid stenosis: ultrasound, magnetic resonance imaging, and computed tomography angiography], Nippon Geka Gakkai Zasshi 112 (6) (2011) 371–376.

[3] S. Cetin, A. Demir, A. Yezzi, M. Degertekin, G. Unal, Vessel tractography using an intensity based tensor model with branch detection, IEEE Trans. Med. Imaging 32 (2) (2013) 348–363.

[4] S. Moccia, E. De Momi, S. El Hadji, L.S. Mattos, Blood vessel segmentation algorithms – review of methods, datasets and evaluation metrics, Comput. Methods Prog. Biomed. 158 (2018) 71–91.

[5] D. Kumar, A. Pramanik, S.S. Kar, S.P. Maity, Retinal blood vessel segmentation using matched filter and Laplacian of gaussian, in: International Conference on Signal Processing and Communications, IEEE, 2016.

[6] N. Memari, A.R. Ramli, M.I.B. Saripan, S. Mashohor, M. Moghbel, Supervised retinal vessel segmentation from color fundus images based on matched filtering and adaboost classifier, PLoS One 12 (12) (2017) e0188939.

[7] F. Zana, J.C. Klein, Segmentation of vessel-like patterns using mathematical morphology and curvature evaluation, IEEE Trans. Image Process. 10 (7) (2001) 1010–1019.

[8] A. Kerkeni, A. Benabdallah, A. Manzanera, M.H. Bedoui, A coronary artery segmentation method based on multiscale analysis and region growing, Comput. Med. Imaging Graph. 48 (2016) 49–61.

[9] Y. Qian Zhao, X. Hong Wang, X. Fang Wang, F.Y. Shih, Retinal vessels segmentation based on level set and region growing, Pattern Recognit. 47 (7) (2014) 2437–2446.

[10] F. Zhao, Y. Chen, Y. Hou, X. He, Segmentation of blood vessels using rule-based and machine-learning-based methods: a review, Multimed. Syst. 25 (2) (2019) 109–118, doi:10.1007/s00530-017-0580-7.

[11] C. Thanapong, W. Watcharachai, R. Somporn, P. Chuchart, S. Manas, Extraction blood vessels from retinal fundus image based on fuzzy c-median clustering algorithm, in: In Fourth International Conference on Fuzzy Systems and Knowledge Discovery (FSKD 2007), 2, IEEE, 2007, pp. 144–148. August

[12] G. Ayala, T. Len, V. Zapater, Different averages of a fuzzy set with an application to vessel segmentation, IEEE Trans. Fuzzy Syst. 13 (3) (2005) 384–393.

[13] X. Zhu, Z. Xue, X. Gao, Y. Zhu, S.T. Wong, Voles: Vascularity-oriented level set algorithm for pulmonary vessel segmentation in image guided intervention therapy, in: In 2009 IEEE International Symposium on Biomedical Imaging: From Nano to Macro, IEEE, 2009, pp. 1247–1250. June

[14] K.W. Sum, P.Y. Cheung, Vessel extraction under non-uniform illumination: a level set approach, IEEE Trans. Biomed. Eng. 55 (1) (2007) 358–360.

[15] Y.Q. Zhao, X.H. Wang, X.F. Wang, F.Y. Shih, Retinal vessels segmentation based on level set and region growing, Pattern Recognit. 47 (7) (2014) 2437–2446.

[16] C. Li, C. Xu, C. Gui, M.D. Fox, Distance regularized level set evolution and its application to image segmentation, IEEE Trans. Image Process. 19 (12) (2010) 3243–3254.

[17] Q. Liu, M. Jiang, P. Bai, G. Yang, A novel level set model with automated initialization and controlling parameters for medical image segmentation, Comput. Med. Imaging Graph. 48 (2016) 21–29.

[18] T. Wan, X. Shang, W. Yang, J. Chen, D. Li, Z. Qin, Automated coronary artery tree segmentation in X-ray angiography using improved hessian based enhancement and statistical region merging, Comput. Methods Prog. Biomed. 157 (2018) 179–190.

[19] H. Tek, M.A. Gulsun, S. Laguitton, L. Grady, D. Lesage, G. Funka-Lea, Automatic coronary tree modeling, Insight J. 1 (8) (2008).

[20] C. Bauer, H. Bischof, Edge based tube detection for coronary artery centerline extraction, Insight J. 1 (7) (2008).

[21] S. Zambal, J. Hladuvka, A. Kanitsar, K. Bähler, Shape and appearance models for automatic coronary artery tracking, Insight J. 4 (2008).

[22] R. Manniesing, M.A. Viergever, W.J. Niessen, Vessel axis tracking using topology constrained surface evolution, IEEE Trans. Med. Imaging 26 (3) (2007) 309–316.

[23] A. Khare, U.S. Tiwary, Soft-thresholding for denoising of medical images – a multiresolution approach, Int. J. Wavel. Multiresolution Inf. Process. 03 (04) (2005) 477–496.

[24] D.H. Trinh, M. Luong, F. Dibos, J.M. Rocchisani, C.D. Pham, T.Q. Nguyen, Novel example-based method for super-resolution and denoising of medical images, IEEE Trans. Image Process. 23 (4) (2014) 1882–1895.

[25] U. Vovk, F. Pernus, B. Likar, A review of methods for correction of intensity inhomogeneity in MRI, IEEE Trans. Med. Imaging Mi 26 (3) (2007) 405–421.

[26] S. Cetin, G. Unal, A higher-order tensor vessel tractography for segmentation of vascular structures, IEEE Transactions on medical imaging 34 (10) (2015) 2172–2185.

[27] J. Zhang, H. Li, Q. Nie, L. Cheng, A retinal vessel boundary tracking method based on Bayesian theory and multi-scale line detection, Comput. Med. Imaging Graph. 38 (6) (2014) 517–525.

[28] Shih-Feng, Yang, Ching-Hsue, Cheng, Fast computation of hessian-based enhancement filters for medical images, Comput. Methods ProgBiomed. 116 (3) (2014) 215–225.

[29] R. Poli, G. Valli, An algorithm for real-time vessel enhancement and detection, Comput. Methods Prog. Biomed. 52 (1) (1997) 1–22.

[30] Ariel, Fernńdez, L. Jorge, Flores, Julia, et al., Image segmentation by nonlinear filtering of optical hough transform, Appl. Opt. 55 (13) (2016) 3632–3638.

[31] C. Bauer, T. Pock, E. Sorantin, H. Bischof, R. Beichel, Segmentation of interwoven 3D tubular tree structures utilizing shape priors and graph cuts, Med. Image Anal. 14 (2) (2010) 172–184.

[32] D. Breitenreicher, M. Sofka, S. Britzen, S.K. Zhou, Hierarchical discriminative framework for detecting tubular structures in 3D images, in: International Conference on Information Processing in Medical Imaging, Springer, Berlin, Heidelberg, 2013.

[33] S.R. Aylward, E. Bullitt, Initialization, noise, singularities, and scale in height ridge traversal for tubular object centerline extraction, IEEE Trans. Med. Imaging 21 (2) (2002) 61–75.

[34] Y. Xu, H. Zhang, H. Li, G. Hu, An improved algorithm for vessel centerline tracking in coronary angiograms, Comput. Methods Prog. Biomed. 88 (2) (2007) 131–143.

[35] Y. Kitamura, Y. Li, W. Ito, Automatic coronary extraction by supervised detection and shape matching, in: 2012 9th IEEE International Symposium on Biomedical Imaging (ISBI), IEEE, 2012, pp. 234–237. May

[36] C. Zhou, H.P. Chan, A. Chughtai, S. Patel, L.M. Hadjiiski, J. Wei, E.A. Kazerooni, Automated coronary artery tree extraction in coronary CT angiography using a multiscale enhancement and dynamic balloon tracking (MSCAR-DBT) method, Comput. Med. Imaging Graph. 36 (1) (2012) 1–10.

[37] B.C. Ramsey, F. Emilio, A.D. Choi, K.R. Branch, D.M. Thomas, Myocardial assessment with cardiac CT: ischemic heart disease and beyond, Curr. Cardiovasc. Imaging Rep. 11 (7) (2018) 16.

[38] T.J. Kim, D.H. Han, K.N.J. And, K.W. Lee, Lung cancer detected at cardiac CT: prevalence, clinicoradiologic features, and importance of full–field-of-view images, Radiology 255 (2) (2010) 369–376.

[39] G.D. Rubin, J. Leipsic, U.J. Schoepf, D. Fleischmann, S. Napel, CT angiography after 20 years: a transformation in cardiovascular disease characterization continues to advance, Radiology 271 (3) (2014) 633–652.

[40] S. Jan-Erik, G. Brian, Advances in cardiac CT contrast injection and acquisition protocols, Cardiovasc. Diagn. Therapy 7 (5) (2017) 439–451.

[41] Y. Bae, Intravenous contrast medium administration and scan timing at CT: considerations and approaches, Radiology 256 (1) (2010) 32–61.

[42] A. Buades, B. Coll, J.M. Morel, A non-local algorithm for image denoising, in: In 2005 IEEE Computer Society Conference on Computer Vision and Pattern Recognition (CVPR'05), 2, IEEE, 2005, pp. 60–65. June

[43] S. Noviano, Y. Suzuki, J. Maeda, Near optimum estimation of local fractal dimension for image segmentation, Pattern Recognit. Lett. 24 (1-3) (2003) 365–374.

[44] Z. Wang, A.C. Bovik, H.R. Sheikh, E.P. Simoncelli, Image quality assessment: from error visibility to structural similarity, IEEE Trans. Image Process. 13 (4) (2004) 600–612, doi:10.1109/tip.2003.819861.

[45] Y. Chang, L. Yan, M. Chen, H. Fang, S. Zhong, Two-stage convolutional neural network for medical noise removal via image decomposition, IEEE Trans. Instrum. Meas. 99 (2019). 1–1

[46] Z.D. Wu, W.X. Xie, J.P. Yu, Fuzzy c-means clustering algorithm based on kernel method, in: In Proceedings Fifth International Conference on Computational Intelligence and Multimedia Applications. ICCIMA 2003, IEEE, 2003, pp. 49–54. September

[47] S. Jan-Erik, G. Brian, Advances in cardiac CT contrast injection and acquisition protocols, Cardiovasc. Diagn. Therapy 7 (5) (2017) 439.

[48] M. Schaap, C. Metz, T.V. Walsum, A.G. Giessen, A.C. Weustink, N. Mollet, C. Bauer, H. Bogunovic, C. Castro-Gonzalez, X. Deng, E. Dikici, T. O'Donnell, M. Frenay, O. Friman, M.H. Hoyos, P.H. Kitslaar, K. Krissian, C. Kühnel, M.A. Luengo-Oroz, M. Orkisz, O. Smedby, M. Styner, A. Szymczak, H. Tek, C. Wang, S.K. Warfield, S. Zambal, Y. Zhang, G.P. Krestin, W.J. Niessen, Standardized evaluation methodology and reference database for evaluating coronary artery centerline extraction algorithms, Med. Image Anal. 13 (5) (2009) 701–714.

[49] Y. Zhang, B.J. Matuszewski, L.K. Shark, C.J. Moore, Medical image segmentation using new hybrid level-set method, in: In 2008 Fifth International Conference Biomedical Visualization: Information Visualization in Medical and Biomedical Informatics, IEEE, 2008, pp. 71–76. July

[50] D. Han, N.T. Doan, H. Shim, B. Jeon, H. Lee, Y. Hong, A fast seed detection using local geometrical feature for automatic tracking of coronary arteries in CTA, Comput. Methods Prog. Biomed. 117 (2) (2014) 179–188.

[51] L. Yu, J. Cheng, Q. Dou, X. Yang, H. Chen, J. Qin, P. Heng, Automatic 3ED cardiovascular MR segmentation with densely-connected volumetric convnets, 2017. ArXiv abs/1708.00573

[52] Y. Shen, Z. Fang, Y. Gao, N. Xiong, C. Zhong, X. Tang, Coronary arteries segmentation based on 3D FCN with attention gate and level set function, IEEE Access 7 (2019) 42826–42835.

[53] D. Lesage, E.D. Angelini, I. Bloch, G. Funka-Lea, A review of 3D vessel lumen segmentation techniques: models, features and extraction schemes, Med. Image Anal. 13 (6) (2009) 819–845.

[54] J. Kang, S. Heo, W.J. Hyung, J.S. Lim, S. Lee, Three-dimensional active vessel tracking using an elliptical prior, IEEE Transactions on Image Processing 27 (12) (2018) 5933–5946.

[55] T. Jerman, F. Pernu, B. Likar, I. Piclin, Enhancement of vascular structures in 3D and 2Dangiographic images, IEEE Trans. Med. Imaging 35 (9) (2016) 2107–2118.

[56] D.M. Baboiu, G. Hamarneh, Vascular bifurcation detection in scale-space, in: 2012 IEEE Workshop on Mathematical Methods in Biomedical Image Analysis, IEEE, 2012, pp. 41–46. January

[57] F. Yuan, Y. Chi, S. Huang, J. Liu, Modeling n-furcated liver vessels from a 3-D-segmented volume using hole-making and subdivision methods, IEEE Trans. Biomed. Eng. 59 (2) (2011) 552–561.

[58] C. Jaquet, L. Najman, H. Talbot, L. Grady, M. Schaap, B. Spain, C.A. Taylor, Generation of patient-specific cardiac vascular networks: a hybrid image-based and synthetic geometric model, IEEE Trans. Biomed. Eng. 66 (4) (2018) 946–955.

[59] H. Zhou, P. Sun, S. Ha, D. Lundine, G. Xiong, Watertight modeling and segmentation of bifurcated coronary arteries for blood flow simulation using CT imaging, Comput. Med. Imaging Graph. 53 (2016) 43–53.

[60] S. Zheng, J. Guo, X. Cui, R.N. Veldhuis, M. Oudkerk, P.M. van Ooijen, Automatic pulmonary nodule detection in CT scans using convolutional neural networks based on maximum intensity projection, IEEE Trans. Med. Imaging 39 (3) (2019) 797–805.